UNIVERSITY OF BIRMINGHAM
University of Birmingham Research at Birmingham

Oxygen hole formation controls stability in LiNiO2 cathodes

Genreith-Schriever, Annalena R.; Banerjee, Hrishit; Menon, Ashok S.; Bassey, Euan N.; Piper, Louis F.j.; Grey, Clare P.; Morris, Andrew J.

DOI:
10.1016/j.joule.2023.06.017

License:
Creative Commons: Attribution (CC BY)

Document Version
Publisher's PDF, also known as Version of record

Citation for published version (Harvard):
Genreith-Schriever, AR, Banerjee, H, Menon, AS, Bassey, EN, Piper, LFJ, Grey, CP & Morris, AJ 2023, 'Oxygen hole formation controls stability in LiNiO2 cathodes', *Joule*, vol. 7, no. 7, pp. 1623-1640. https://doi.org/10.1016/j.joule.2023.06.017

Link to publication on Research at Birmingham portal

General rights
Unless a licence is specified above, all rights (including copyright and moral rights) in this document are retained by the authors and/or the copyright holders. The express permission of the copyright holder must be obtained for any use of this material other than for purposes permitted by law.

•Users may freely distribute the URL that is used to identify this publication.
•Users may download and/or print one copy of the publication from the University of Birmingham research portal for the purpose of private study or non-commercial research.
•User may use extracts from the document in line with the concept of 'fair dealing' under the Copyright, Designs and Patents Act 1988 (?)
•Users may not further distribute the material nor use it for the purposes of commercial gain.

Where a licence is displayed above, please note the terms and conditions of the licence govern your use of this document.

When citing, please reference the published version.

Take down policy
While the University of Birmingham exercises care and attention in making items available there are rare occasions when an item has been uploaded in error or has been deemed to be commercially or otherwise sensitive.

If you believe that this is the case for this document, please contact UBIRA@lists.bham.ac.uk providing details and we will remove access to the work immediately and investigate.

Download date: 28. Apr. 2024

Joule

CellPress
OPEN ACCESS

Article

Oxygen hole formation controls stability in $LiNiO_2$ cathodes

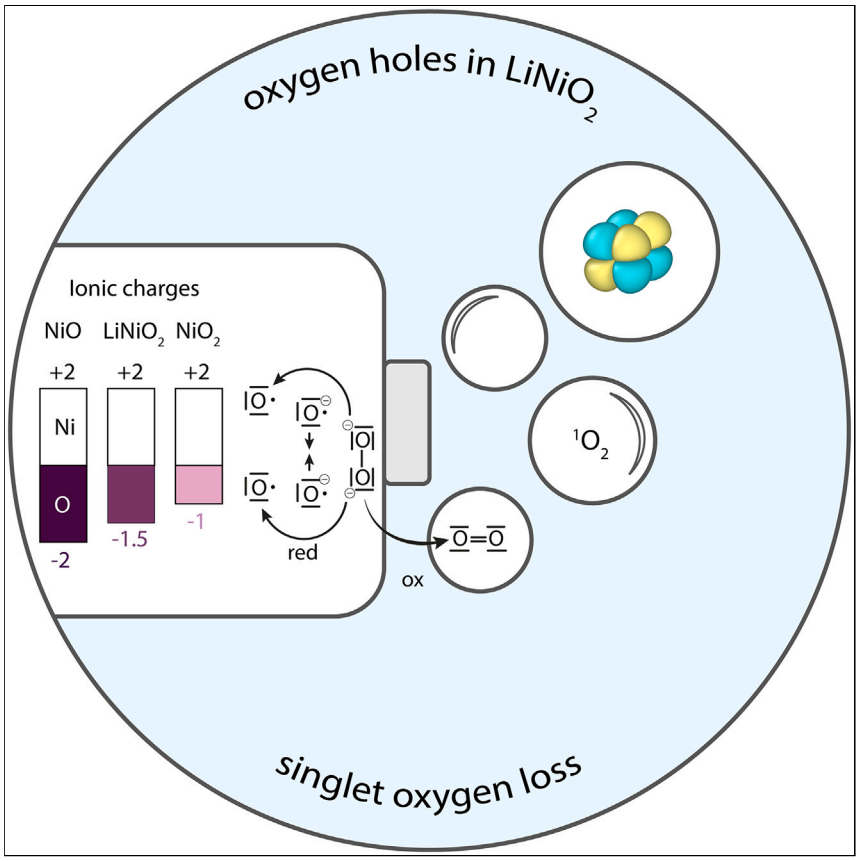

The energy density of Li-ion batteries can be increased using high-voltage cathode materials such as Ni-rich layered oxides. These cathodes, however, are known to lose oxygen, causing electrolyte oxidation and battery failure. Our work provides a comprehensive understanding of both bulk and surface oxygen "Ni–O" redox reactions, providing a mechanism for singlet oxygen release in $LiNiO_2$ and highlighting the role of O redox in these processes. The findings provide insights into how to mitigate degradation in future cathode materials.

Annalena R. Genreith-Schriever, Hrishit Banerjee, Ashok S. Menon, Euan N. Bassey, Louis F.J. Piper, Clare P. Grey, Andrew J. Morris

cpg27@cam.ac.uk (C.P.G.)
a.j.morris.1@bham.ac.uk (A.J.M.)

Highlights

Dominant O-redox contributions to Ni–O redox in $LiNiO_2$ and oxygen holes

Excellent agreement between predicted and experimental X-ray absorption spectra

Reaction pathway of oxygen evolution via peroxide intermediate

Spin conservation of peroxide ground-state singlet causes release of singlet oxygen

Genreith-Schriever et al., Joule 7, 1623–1640
July 19, 2023 © 2023 The Author(s). Published by Elsevier Inc.
https://doi.org/10.1016/j.joule.2023.06.017

Joule

CellPress
OPEN ACCESS

Article

Oxygen hole formation controls stability in $LiNiO_2$ cathodes

Annalena R. Genreith-Schriever,[1,5] Hrishit Banerjee,[1,2,5] Ashok S. Menon,[3,5] Euan N. Bassey,[1,4,5] Louis F.J. Piper,[3,5] Clare P. Grey,[1,5,*] and Andrew J. Morris[2,5,6,*]

SUMMARY

Ni-rich lithium-ion cathode materials achieve both high voltages and capacities but are prone to structural instabilities and oxygen loss. The origin of the instability lies in the pronounced oxidation of O during delithiation: for $LiNiO_2$, NiO_2, and the rock salt NiO, density functional theory and dynamical mean-field theory calculations based on maximally localized Wannier functions yield a Ni charge state of *ca.* +2, with O varying between −2 (NiO), −1.5 ($LiNiO_2$), and −1 (NiO_2). Calculated X-ray spectroscopy Ni *K* and O *K*-edge spectra agree well with experimental spectra. Using *ab initio* molecular dynamics simulations, we observe loss of oxygen from the (012) surface of delithiated $LiNiO_2$, two surface $O^{\bullet-}$ radicals combining to form a peroxide ion, and the peroxide ion being oxidized to form O_2, leaving behind two O vacancies and two O^{2-} ions. Preferential release of $^1O_2$ is dictated via the singlet ground state of the peroxide ion and spin conservation.

INTRODUCTION

Ni-rich layered oxides exhibit excellent performance as high-voltage cathode materials, enabling batteries with high energy densities, and are widely used in current electric vehicle batteries.[1,2] They are, however, prone to structural instabilities and degradation involving oxygen loss[3–6]—the degradation being particularly pronounced as the Ni content increases, hampering the development of Co-free next-generation cathode materials. The thermal evolution of singlet oxygen $^1O_2$ from delithiated Ni-rich cathode materials has been captured experimentally,[7] and its electrochemical formation has been inferred from the large amount of electrolyte oxidation products that accompany electrode degradation, which are unlikely to be caused by direct reaction with unreactive triplet oxygen.[8,9] Neither the reason for singlet formation nor its fate after evolution from the surface is, to date, well understood.

At the heart of the O-loss problem is the role that O vs. Ni redox plays in the partially reversible removal and reinsertion of Li. The redox activity of $LiNiO_2$ (LNO) is generally attributed predominantly to Ni, i.e., it is assumed that in the process of charging and discharging the battery, it is mainly the Ni cation that is oxidized and reduced.[5,10–13] Within the formal oxidation state (ionic) model, Ni is considered to be oxidized from +3 to +4 upon delithiating LNO.[5,13] It is clear that this ionic picture does not fully capture the nature of the Ni–O bonds, which are known to exhibit covalent character with hybridization between the Ni *d* and O *p* states. The charge states of both species will therefore deviate from their formal oxidation states.[10,14] However, the consensus is generally that Ni is not solely oxidized/reduced and

CONTEXT & SCALE

High Ni content layered transition metal oxides enable lithium-ion batteries with high operating voltages but are prone to degradation. Electrolyte oxidation results as the material is delithiated, along with oxygen evolution and surface reconstructions of the cathodes. Mitigating these phenomena requires a comprehensive understanding of the relevant processes. We here propose that a major source of these instabilities arises from the oxide anion oxidation on delithiation: "Ni" redox processes occur whereby essentially all of the charge is removed from the O ions directly bound to Ni. Our simulations show that the surface $O^{\bullet-}$ radicals formed during the redox processes combine to form peroxide ions, and these disproportionate to form molecular oxygen and oxygen anions. The ground-state singlet of the peroxide intermediate governs the release of singlet oxygen via spin conservation. This understanding of bulk/surface reaction mechanisms provides insights into how to maximize the performance and lifetime of future cathodes.

This is an open access article under the CC BY license (http://creativecommons.org/licenses/by/4.0/).

that although O is somewhat involved in the Ni–O redox processes, Ni activity remains dominant. In agreement with this,[5,10,11] X-ray spectroscopy (XAS) of Ni-rich layered oxides shows a shift of the Ni *K* edge on delithiation toward higher energies,[11,15–17] which is commonly interpreted as experimental confirmation of the changes in the Ni charge state, but Menon et al.,[17] however, suggests that full oxidation to form Ni^{4+} does not occur. Kong et al.[10] have previously reported partial O oxidation upon delithiation of LNO but continue to attribute the main redox activity to Ni. In a similar vein, Korotin et al.[18] and Foyevtsova et al.[19] invoke ligand holes on oxygen, suggesting a partial charge transfer of oxygen to Ni but simultaneously propose a disproportionation of the Ni charge states, a process that has not yet been confirmed experimentally. A greater involvement of O is considered in O-redox materials, where O redox goes beyond σ(Ni–O) interactions, e.g., in Li-excess cathode materials,[14,20–23] in the form of orphaned O states[14] or stabilizing delocalized metal-oxygen π interactions.[20] To date, little work has considered the role that the rehybridization of Ni–O bonds plays in oxygen loss in non-Li-excess layered oxides.[17,24–26] This is the focus of this work.

The charge states in the LNO system have not previously been investigated in depth, especially as there are numerous technical challenges regarding the quantification of species in hybridized states. Wave-function-based charge analyses proposed, for example, by Mulliken[27] partition the wave function according to atomic orbitals, which is a questionable approach for characterizing hybridized states. Determining oxidation states using density functional theory (DFT) calculations requires the ground-state electron density to be partitioned and assigned to the individual ions; therefore, the resulting ionic charge often depends on the choice of partitioning scheme, the most established being Bader charge analysis.[28] Reeves and Kanai[29] as well as Quan and Pickett[30] suggest that projecting the DFT charge density onto maximally localized Wannier functions yields the most reliable charges of atoms in molecules[29] and ions in crystals.[30] This is the approach that is applied in this work.

To understand the role of the surface itself in singlet oxygen formation, Wandt et al.[7] have studied thermally induced O_2 evolution from Ni-rich layered oxides into the gas phase. They report a rise in $^1O_2$ evolution around 500 K, confirming the existence of at least one route for $^1O_2$ formation without any electrolyte. Houchins et al.[31] have recently proposed that in metal-air batteries, singlet oxygen forms via a disproportionation reaction of superoxide radicals in solution. As the superoxide radicals are part of the metal-air electrochemistry and they play no direct role in Li-ion batteries, it is unlikely or at least unclear if the formation of singlet oxygen in Li-ion batteries with layered oxide cathode materials follows the same pathway.

Understanding how oxygen is evolved requires an atomistic examination of the surfaces involved. Based on scanning electron microscopy and X-ray diffraction, Zhu and Chen[32] and Garcia et al.[33] showed that the prevalent surfaces in Ni-rich layered oxide cathodes are the (012), (001), and (104) families, in line with computational predictions.[34–36] The facets found to cover the greatest surface area, over a range of particle morphologies, were (012) facets,[32] which are predicted to be O terminated at synthesis conditions.[34] The O-terminated (012) facet is therefore an ideal model system to explore (singlet) oxygen loss in Ni-rich layered oxides.

Here, we re-examine the classic picture of transition metal-centered redox in stoichiometric $LiNiO_2$ and delithiated NiO_2. At high states of charge, LNO is known to decompose, forming surface reconstruction phases with rock salt-like structures,[5,37]

[1]Yusuf Hamied Department of Chemistry, University of Cambridge, Cambridge CB2 1EW, UK

[2]School of Metallurgy and Materials, University of Birmingham, Birmingham B15 2TT, UK

[3]WMG, University of Warwick, Coventry CV4 7AL, UK

[4]Materials Department and Materials Research Laboratory, UC Santa Barbara, Santa Barbara, CA 93106, USA

[5]The Faraday Institution, Harwell Science and Innovation Campus, Didcot OX11 0RA, UK

[6]Lead contact

*Correspondence: cpg27@cam.ac.uk (C.P.G.), a.j.morris.1@bham.ac.uk (A.J.M.)

https://doi.org/10.1016/j.joule.2023.06.017

the prototype material of which, NiO, is studied here. A variety of computational tools ranging from DFT to dynamical mean-field theory (DMFT) calculations are employed to determine oxidation states. We use charge analysis schemes ranging from a Bader charge analysis to the Wannier transformation and integration over the impurity Green's functions within DMFT, an approach that promises to become a powerful tool for analyzing charge states in battery materials. We validate our predictions against experiment by predicting the XAS spectra at the Ni *K* and O *K* edges of LNO and NiO_2 and comparing them with previously published experimental Ni *K* and O *K*-edge X-ray spectra of $LiNiO_2$ at varying states of delithiation.[17] Employing *ab initio* molecular dynamics (AIMD) simulations, we analyze the spontaneous O_2 release from the (012) surface of delithiated LNO and, for the first time, computationally capture singlet oxygen as it forms at the cathode surface. We propose a comprehensive mechanism for the observed route of oxygen loss and singlet oxygen formation, pivotal for mitigating electrolyte oxidation pathways associated with singlet oxygen release.[38]

RESULTS

Oxidation states

Even at the most basic level of charge analysis, a Bader partition of DFT densities from PBE + *U* calculations (U_{eff} = 6 eV, as proposed by Das et al.[5] and validated with hybrid functionals and DMFT in this study) shows that Ni exhibits a similar charge state in materials that show three different formal Ni oxidation states: NiO, $LiNiO_2$, and NiO_2 (see Figure 1A, first blue bar in each set). By contrast, Figure 1A shows that the O charge state, on the other hand, changes significantly upon delithiation of $LiNiO_2$ and even further upon the formation of NiO. The electronic density of states (DOS) (see Figure 1B) suggests ferromagnetic behavior at 0 K. Of particular interest are the states just below the Fermi energy, as these are the states that electrons are removed from upon delithiation of the material. The character of these states can be estimated by projecting the DOS onto spherical harmonics, i.e., local atomic orbitals. They indicate that the states just below the Fermi energy have predominantly O (red) contributions and only to a small extent Ni (blue) contributions. The charge density of these states (yellow isosurface in Figure 1C) confirms pronounced O *p* contributions and weaker Ni e_g contributions just below the Fermi energy (the states are highlighted in the DOS in Figure 1B).

Due to the hybridized nature of the states near the Fermi energy and the challenges in separating the charges, the charges were also analyzed at a more advanced level with the Wannierization of PBE Kohn-Sham orbitals. In the case of LNO, Ni *d* Wannierization shows large O *p* contributions for the nominal Ni e_{g^*} states or highest occupied states (orbitals shown in yellow and green in Figure 1C), confirming that the Ni and O bands are strongly hybridized. The electronic band structure (see Figure S2 in supplemental information) suggests that the Ni *d* and O *p* bands are very close in energy, requiring both states to be included in the correlated subspace of the Wannierization. If the O states are explicitly included in the Wannierization using a *d-p* model, Ni *d* states are localized on Ni centers and O *p* states on O centers (see Figure 1C; the Wannierization process also identifies the orientation of the charge density lobes, allowing the Wannier functions to be plotted relative to a global coordinate system). NiO_2 also requires a *d-p* model, while NiO contains *d* and *p* bands that are well separated, making a *d* model sufficient (see band structure in Figure S2 of supplemental information and additional NiO *d-p* analysis in Figure S3). The resulting ionic charges calculated from Wannier occupancies (see Figure 1A, middle bar in each set) have significantly larger values than the Bader charges (by 0.5–0.8

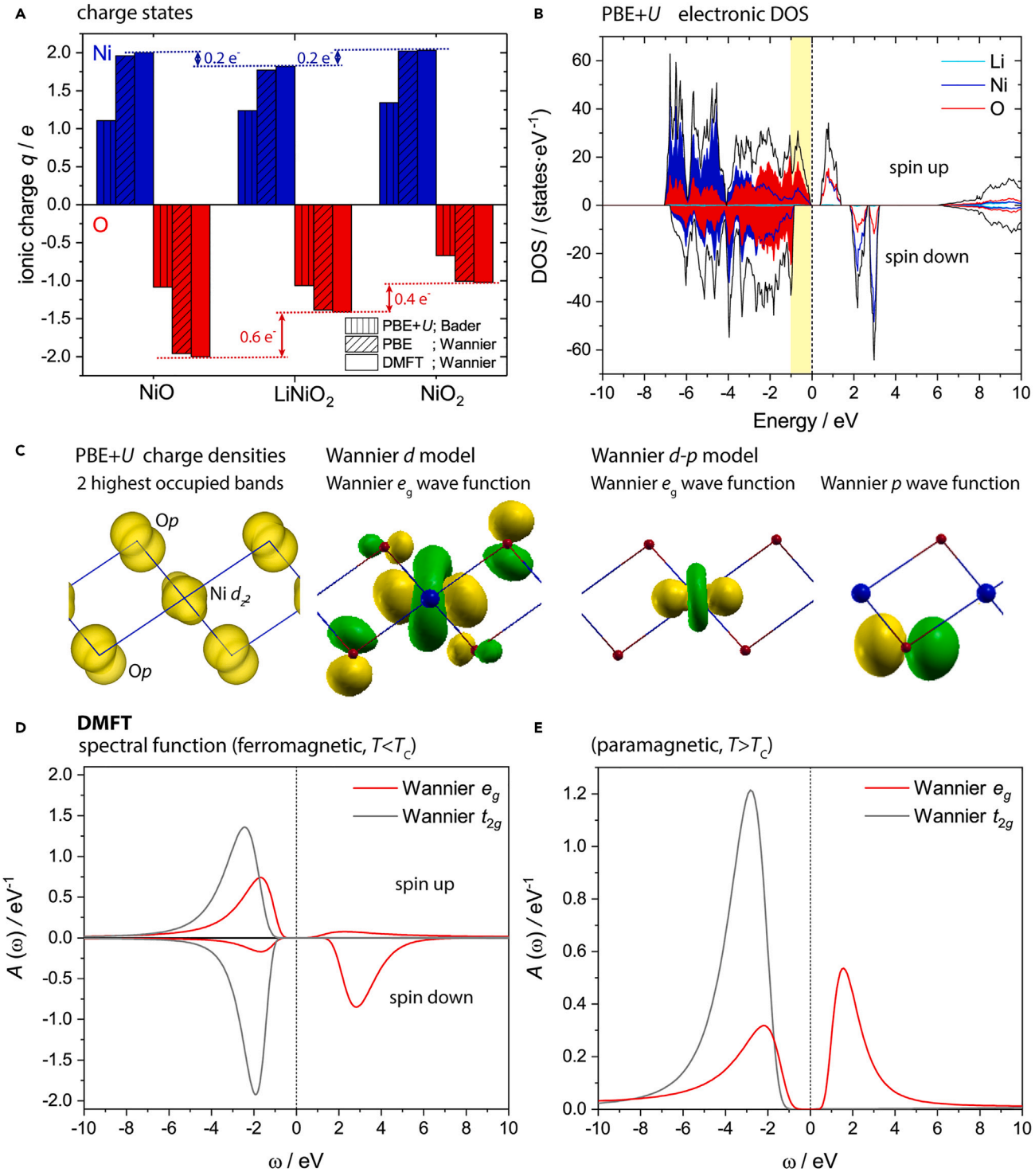

Figure 1. Oxidation states in $LiNiO_2$ and related materials and $LiNiO_2$ electronic structure

(A) Ionic charges of Ni (blue) and O (red) in NiO, $LiNiO_2$, and NiO_2 determined with PBE + U (U_{eff} = 6 eV) and a Bader analysis (left bar in each set), Wannier occupancies based on PBE Bloch states (middle bar), and full charge self-consistent DFT + DMFT based on Wannierization (right bar).

(B) PBE + U electronic DOS of $LiNiO_2$ with Ni contributions shown in blue and O contributions shown in red. The highest occupied states are highlighted in yellow. They indicate strong O contributions.

(C–E) Charge density and Wannier functions of $LiNiO_2$, the yellow isosurface shows the charge density of the highest occupied states, as obtained from PBE + U calculations for E_F − 1 eV to E_F, and the yellow and green isosurfaces depict the Wannier wave functions after rotation relative to a global

Figure 1. *Continued*

coordinate system. The Wannier *d* wavefunctions obtained from a Ni *d* model of LNO show Ni d_{z^2} character and significant contributions from O *p* states, which are moved to an O center if the O *p* states are explicitly included in the active basis set. The spectral functions obtained from a DMFT impurity model of Ni for (D and E) the ferromagnetic material at $T < T_C$ (O is treated as part of the electron bath in the DMFT calculations) (D) and the paramagnetic material at $T > T_C$ (E), showing good agreement with the small band-gap paramagnetic character seen in experiment.[39–44]

e in the case of Ni and 0.3–0.9 *e* in the case of O) but confirm all trends seen with the Bader analysis of the PBE + *U* states; again, the Ni charges are nearly identical in $LiNiO_2$, NiO_2, and NiO, whereas the O oxidation states vary substantially, suggesting pronounced involvement of O in the redox processes.

A question then arises as to whether this O character just below the Fermi energy and the resulting redox activity of O is an artifact, e.g., of the DFT calculations themselves or of the static Hubbard *U* treatment of electron correlation, which lowers the energy of the Ni states, potentially causing unphysical O *p* character just below the Fermi energy. DMFT calculations were therefore performed to address this, which account for electron correlations via a mean-field approach and obtain charge states by integrating over the impurity Green's functions in a Wannier basis. The DMFT spectral function is shown in Figure 1D for the ferromagnetic case, resembling the DFT DOS at 0 K. At temperatures above the Curie temperature, the material becomes paramagnetic, as shown in Figure 1E, where the two e_g states are each half occupied (red line). This small band-gap paramagnetic behavior is in good agreement with experimental findings at battery operating temperatures.[39–43]

Returning to the question of the charge states of Ni and O, Figure 1A shows that the DMFT charges (third bar of each set) are nearly identical to the Wannier charges based on the PBE densities (middle bar of each set). DMFT yields a Ni oxidation state of $\sim +2$ in all three materials, $LiNiO_2$, NiO_2, and NiO, while the charge of O is *ca.* -1.5 in $LiNiO_2$ and -1 in NiO_2 and assumes its most stable state of -2 only in the decomposition product NiO. Note, if a fraction of the Li ions remained in the material at high states of charge, this would have negligible impact on the structure and ionic charges (see Figure S5 in supplemental information).

A standard experimental procedure to track oxidation state changes in battery materials is XAS. To validate the computed charge states and directly compare our predictions with experiment, we calculated Ni *K* and O *K* spectra for LNO and NiO_2 (see Figures 2A and 2B) and compared them with experimental Ni *K* and O K X-ray spectra of a 2% W-doped LNO cathode at varying states of delithiation (see Figures 2C and 2D).[17] The spectra were collected in the bulk-sensitive fluorescent yield mode.

Figure 2A shows a clear shift of the edge position in the calculated Ni *K* spectra, with the calculations yielding a Ni charge state of +2 both in LNO and NiO_2. The magnitude of the shift is in excellent agreement with the edge shift observed in the experiment (see Figure 2C). Although our DFT calculations find that the Ni charge remains at +2, they predict that the local Ni–O bonding environment changes on delithiation (see Figure 2E). In line with previous computations[5,45] and extended X-ray fine structure (EXAFS) results,[46] we find that LNO undergoes Jahn-Teller distortions at 0 K (see Figure S4 for a more detailed discussion of the Jahn-Teller distortions). In distorted $LiNiO_2$, Ni is coordinated by two O ions at a longer distance of 2.1 Å and four O ions at a shorter distance of 1.9 Å. NiO_2, by contrast, is undistorted, with Ni being surrounded by six O ions at a distance of 1.9 Å. Leaving aside changes in the symmetry of the bonding environment, the average bond lengths also change on delithiation, decreasing from 2.0 Å in LNO to 1.9 Å in NiO_2.

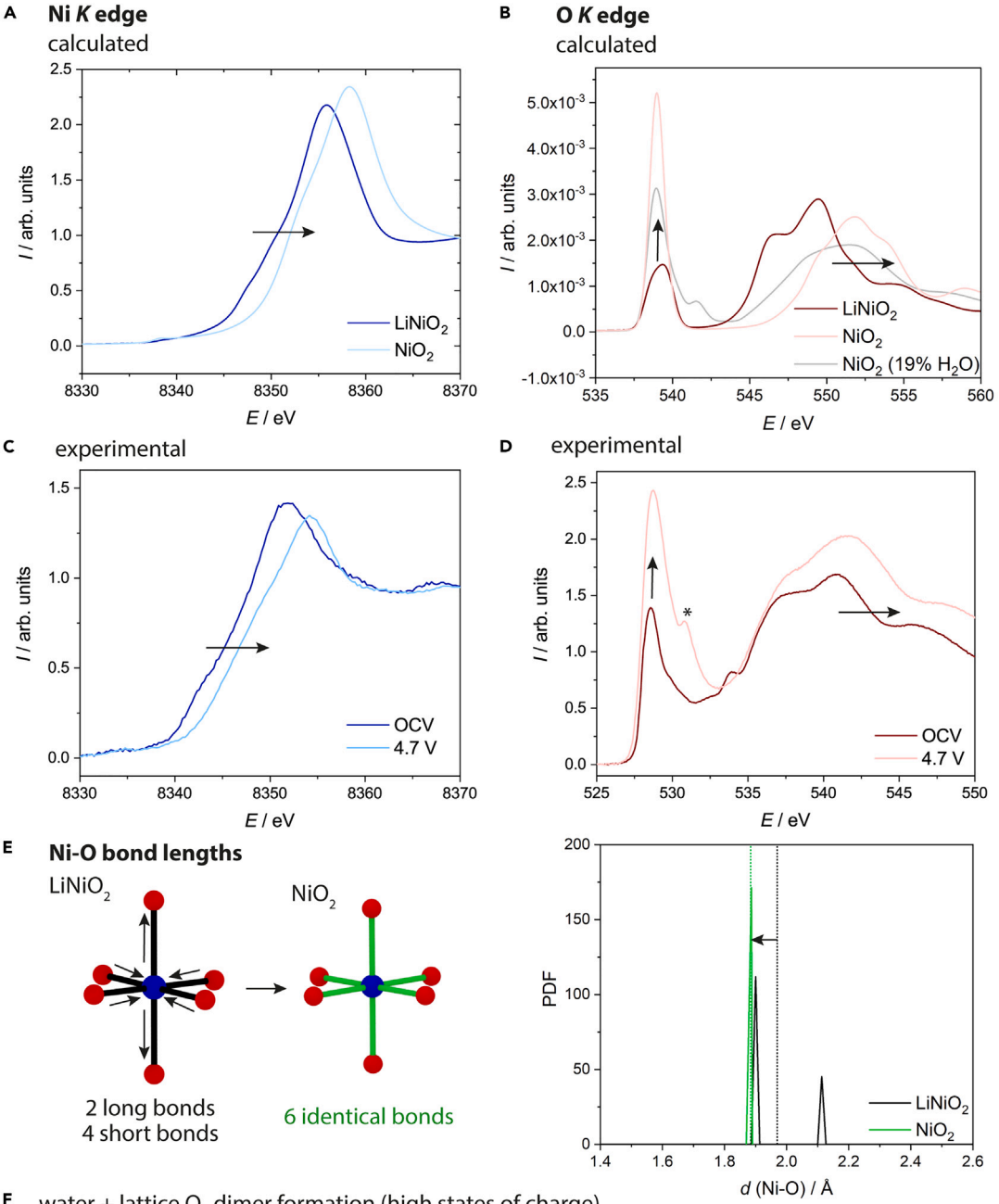
A
Ni K edge
calculated
I / arb. units
E / eV
LiNiO2
NiO2
B
O K edge
calculated
I / arb. units
E / eV
LiNiO2
NiO2
NiO2 (19% H2O)
C
experimental
I / arb. units
E / eV
OCV
4.7 V
D
experimental
I / arb. units
E / eV
OCV
4.7 V
E
Ni-O bond lengths
LiNiO2
NiO2
2 long bonds
4 short bonds
6 identical bonds
PDF
d (Ni-O) / Å
LiNiO2
NiO2
F
water + lattice O2 dimer formation (high states of charge)
16 fs
190 fs
377 fs
O
Ni
H
1.2 Å

Figure 2. X-ray absorption spectra

(A) Calculated Ni *K*-edge spectra of $LiNiO_2$ and NiO_2.

(B) Calculated O *K*-edge spectra of $LiNiO_2$, NiO_2, and hydrated NiO_2.

(C) Experimental Ni *K*-edge spectra of $LiNi_{0.98}W_{0.02}O_2$ at open circuit voltage (OCV) and charged to 4.7 V.

(D) Experimental O *K*-edge spectra of $LiNi_{0.98}W_{0.02}O_2$ at OCV and 4.7 V. The asterisk denotes a signal arising at 531 eV at high states of charge, conventionally assigned to lattice O redox. The peak at 534 eV in the OCV data stems from surface carbonate species. (C) and (D) adapted from Menon et al.[17].

(E) Loss of Jahn-Teller distortions and decrease of the mean Ni–O bond length of LNO on delithiation.

(F) Water-assisted formation of O–O dimers, as obtained from AIMD simulations at different timesteps. The snapshot at 377 fs was used for the prediction of the XAS spectrum of hydrated NiO_2 in (B).

The O *K*-edge spectrum shows overall greater changes on delithiation than the Ni *K* spectrum, both computationally (see Figure 2B) and experimentally (see Figure 2D). Theory and experiment are again in good agreement regarding the evolution of features, showing a pronounced increase of the O pre-edge peak—a measure of the covalency of the Ni–O bonds—as well as an overall shift of the spectrum to higher energies. The onset of the calculated spectra is *ca.* 10 eV higher than that of the experimental spectra due to the single-particle treatment of the O *K* edge (which provides less reliable onset energies than multiple scattering approaches but is the best-suited method to calculate the O *K*-edge spectra, see Figure S7 in supplemental information for a detailed discussion). Calculations performed with W-doped $LiNi_{0.94}W_{0.06}O_2$ and $Ni_{0.94}W_{0.06}O_2$ show that small levels of W incorporation have very little impact on the calculated O *K* spectra (see Figure S7).

A small additional feature at around 531 eV is seen in the experimental O *K* spectrum at a high state of charge that is not seen in the calculated spectrum of either defect-free NiO_2 or $Ni_{0.94}W_{0.06}O_2$. Lee et al.[47] have recently proposed that water can be co-intercalated electrochemically into $LiNiO_2$ in aqueous electrolytes. The question then is, could water be causing the additional XAS feature? Although this requires water to generally be available in the system, the generation of protons at low voltages (from ethylene carbonate (EC) dehydrogenation) and water at higher voltages from the oxidation of protic electrolytes and, in particular, EC, is well established for Ni-rich layered lithium nickel manganese cobaltates (NMCs).[48] These oxidative processes have been proposed to result in protonated NMC surfaces,[48] and more generally, proton insertion into layered cathode materials is also well established,[49–51] as is the intercalation of water, particularly for some partially oxidized layered Na-containing cathode materials.[52] AIMD simulations of hydrated LNO were therefore performed at varying states of delithiation. At high states of charge, water molecules intercalated into NiO_2 react with lattice O to form O–O dimers with a bond length of *ca.* 1.2 Å (see Figures 2F and S6 of supplemental information). Some of the dimers and the nearby lattice O are protonated, with dynamic proton exchange occurring. The dimers do not leave the lattice sites in the course of our simulations. A systematic investigation of the process and a potential involvement of electronic quasi-particles that could, in principle, give rise to a similar feature (see Figure S7) is underway, but it is worth noting at this stage, first, that the O–O dimers yield XAS signals matching the additional high-voltage feature seen experimentally (see Figures 2B and 2D) and, second, that an XAS spectrum calculated for the hydrated material shows excellent overall agreement with the experimental spectrum at 4.7 V.

Surface oxygen loss

As LNO is known to decompose through surface reactions, it is pivotal to understand how the bulk oxidation states discussed above compare to oxidation state and charge density changes at the surface. We explore the prevalent (012) facet,[32,33] where Li is

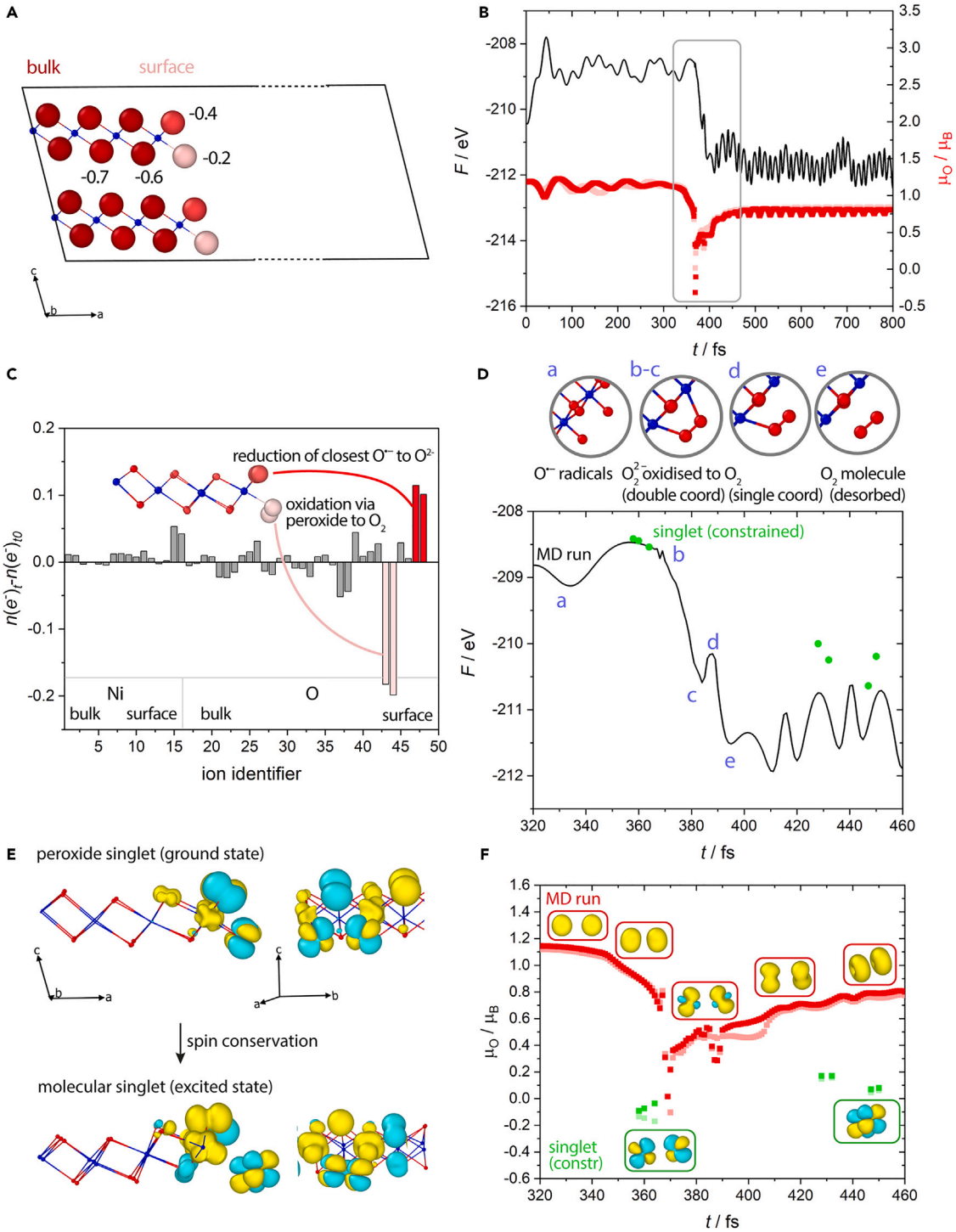

Figure 3. Mechanistic analysis of the observed route of O_2 evolution and the formation of $^1O_2$

(A) Oxidation states of the O ions on and near the (012) facet of NiO_2 according to a Bader charge analysis of the PBE + *U* charge density; lighter colors represent higher states of oxidation. Surface O ions are in a yet more oxidized state than bulk O.

(B) Free energy profile (black) and magnetic moments of surface O species (red) of a route of spontaneous O_2 loss, as found in AIMD simulations at *ca.* 450 K. The reaction occurs around 370–400 fs, the free energy decreasing by ca. 3 eV. The magnetic moments suggest radical character at the beginning of the simulation, $\mu_O \approx 1.1\mu_B$, and an abrupt change in electronic character during the reaction.

(C) Differences in electron numbers of all ions in the simulation cell between 389 fs (when O_2 just desorbed) and the start of the simulation based on a Bader analysis.

Figure 3. *Continued*

(D) Closeup of the free energy profile with characteristic points indicated. $O^{\bullet-}$ radicals (a) combine to form a double coordinated peroxide (b), which is continuously oxidized to an O_2 molecule (c–e) and through a single coordinated transition state (d) desorbs as O_2 (e). The charge is transferred to the nearest $O^{\bullet-}$ radicals (see C).

(E) Magnetization density of the peroxide ground-state singlet state and the excited molecular singlet state (yellow isosurfaces denote positive spin density and cyan isosurfaces negative spin density, isosurface levels of $\pm$ 5.3 × 10^{-5} $e/Å^3$).

(F) Closeup of the magnetic moments of the two $O^{\bullet-}$ forming the O_2 molecule as a function of time.

extracted and inserted during cycling, and investigate the fully delithiated, unstable material NiO_2 (see Figures 3A and S8 of supplemental information). Since the analysis of the oxidation states showed that the Bader charge analysis gave the correct relative changes of the oxidation states in bulk $LiNiO_2$ and NiO_2 without the necessity to assess the suitability of different Wannier models, the surface charges of the (012) facet of NiO_2 were evaluated with a Bader charge analysis of the PBE + *U* charge density. This shows that O at the surface is oxidized even further than in the bulk (see Figure 3A). Each Ni–O layer exhibits O species with two slightly different charge states at the surface, both with a lower electron density than in the bulk.

AIMD simulations of the (012) NiO_2 surface show a spontaneous loss of O_2 molecules and even the formation of singlet oxygen in the process (see Figure 3B) at simulated temperatures from 300 to 800 K. Figure 3B shows the free energy profile of an exemplary PBE + *U* trajectory at *ca.* 450 K, indicating that this reaction to release one O_2 molecule liberates 3.0 eV. This was confirmed with AIMD simulations including dispersion interactions and based on hybrid functionals, which also show spontaneous O_2 loss to release *ca.* 3 eV. As seen in Figure 3B, the reaction appears barrierless, suggesting that the activation barrier is smaller than the energy fluctuations due to thermal vibrations (< 0.05 eV).

At the beginning of the simulation, the O species at the surface of NiO_2 are separated by *ca.* 2.8 Å. An analysis of magnetic moments yields *ca.* 1.1 μ_B per O (see Figure 3B), indicating the presence of unpaired electrons. The magnetization density shows no unpaired electrons in the bulk but positive spin density on the surface O that interacts antiferromagnetically with negative spin density on the nearest Ni ions (see Figure S9 in supplemental information), suggesting radical (or hole) character of the surface O, i.e., $O^{\bullet-}$. When lattice vibrations bring two $O^{\bullet-}$ radicals close together (*ca.* 1.4 Å) at 369 fs, the electronic character of the surface O changes, causing a steep decrease of the magnetic moments to *ca.* 0 μ_B, indicative of the formation of a peroxide ion. The charge density and electron localization function show a covalent O–O bond of the dimer (see Figure S11), in agreement with an O_2 dimer predicted by Kong et al.[10] for a different surface, the (104) facet. The O_2 dimer formation Kong et al.[10] report is related to the one observed here but differs in that it requires oxide ions to combine across NiO_2 layers, whereas in the case of the (012) facet, the oxide ions combine with oxide ions from the same NiO_2 layers. We see the dimer formation occurring at both facets but occurring at lower temperatures in the case of the (012) facet. As the (012) facet has also been found to be the prevalent facet experimentally,[32,33] we consider the release reaction from the (012) facet to be the most representative pathway of oxygen release from Ni-rich cathodes.

The moments exhibit a steep decrease around 369 fs to 0, indicating a singlet ground state of the peroxide ion, and steadily increase from *ca.* 0.3 μ_B at 371 fs to *ca.* 0.8 μ_B from 500 fs onward. Once released from the surface, $^1O_2$ is no longer a ground state and looks identical to $^1O_2$ obtained for the gas phase ($^1\Delta$, see Figure S10 in supplemental information). Figure 3C shows the change in electron numbers throughout the reaction, according to a Bader analysis. The O ions forming

the peroxide are oxidized. Although some of the electron density drawn from the peroxide in the oxidation is transferred to the nearest Ni ions, the majority goes to the nearest surface $O^{\bullet -}$ radicals. As the peroxide is oxidized, the O–O distance decreases further to *ca.* 1.2 Å at 384 fs, typical of an O_2 molecule. Figure 3D shows a closeup of the free energy profile. The two $O^{\bullet -}$ radicals (a) form the peroxide at 369 fs (b), which is oxidized continuously to O_2, in double coordination at 384 fs (c), single coordination at 387 fs (d), and desorbed at 394 fs (e), assuming a Ni–O bond cut-off length of 2.05 Å (based on the charge density and electron localization function). Most of the oxidation occurs between (b) and (c). The released oxygen molecule vibrates around an average bond length of 1.2 Å and leaves behind two oxygen vacancies and two reduced surface O ions. The free energy curve shows that *ca.* 1.7 eV (55%) of the free energy gain is due to the peroxide formation and oxidation, while *ca.* 1.3 eV (45%) is due to the remaining oxidation and O_2 desorption. The activation barrier of the desorption is *ca.* 0.04 eV, which can be easily overcome by thermal energy, especially in the light of the large amount of energy released through the peroxide formation. The rate-determining step is therefore most likely the peroxide formation (with a negligible barrier at 450 K).

Singlet oxygen

With this mechanistic understanding of the observed route of oxygen loss from delithiated LNO, we can turn to the question of why singlet oxygen is formed. O_2 molecules in the gas phase have a triplet ground-state $X^3\Sigma^-_g$ separated by an energy gap of *ca.* 0.9 eV from the first excited state (complete active space self consistent field [CASSCF] calculations,[53] experiment[54]), i.e., the singlet $a^1\Delta_g$ state. Higher in energy still is the $b^1\Sigma^+_g$ state, which is generally not observed to react chemically as it physically deactivates quickly into the $^1\Delta$ state. To unravel the mechanism of the singlet formation in our simulations, it is essential to identify $^1O_2$ signatures in the simulations.

The two highest energy electrons of $^1O_2$ are of opposite spin, giving the singlet an overall magnetic moment of zero. AIMD simulations show that, at 369 fs, the magnetic moments of the two oxide radicals forming the peroxide drop and approach zero briefly (see Figures 3B and 3F) before steadily increasing from *ca.* 0.3 μ_B (at 371 fs) to *ca.* 0.8 μ_B (from 500 fs onward). Albeit briefly, this points toward singlet character of the electronic ground state, and this is the ground state of the peroxide ion. Through constraining the number of unpaired electrons in the simulation cell, we can also enforce the singlet state before the transition, and we see it become degenerate with the AIMD ground state (nearly degenerate *ca.* 15 fs before the drop in the magnetic moments and fully degenerate *ca.* 3 fs before the drop; see the green data points in Figures 3D and 3F). This singlet state forms as the two oxide radicals forming the peroxide come close enough together to start interacting with each other but before any oxidation takes place. The magnetization density of the singlet state is illustrated in Figures 3E and 3F. Two states with strong O *p* character are seen, one populated with a spin-up electron and the other with a spin-down electron. The lobes of the negative spin state are slightly larger than the lobes of the positive spin state, resulting in a magnetic moment of *ca.* −0.1 μ_B.

As the simulation proceeds and the peroxide is oxidized, the negative lobes shrink until they disappear, and the magnetic moments increase to 0.8 μ_B (see Figures 3B and 3F), suggesting triplet character of the ground-state $^3O_2$ molecule after it has left the surface. Through constraining the number of unpaired electrons, the singlet state is also obtained for $^1O_2$ after it has left the surface. The magnetization density seen in Figure 3F looks very similar to the singlet seen during the peroxide

formation, but in the $^1O_2$ molecule, the planes of the lobes are fully aligned, suggesting a stronger interaction (at a smaller distance; earlier 1.4 Å between the interacting radicals vs. 1.2 Å in the molecule). Figure 3D shows that the gas phase singlet is no longer degenerate with the ground state but is in an excited state.

In a DFT gas phase calculation, $^1O_2$ can also be obtained by constraining the magnetic moments of each O atom to zero. The gas phase $^1O_2$ shows the same magnetization density as the gas phase $^1O_2$ at the surface of NiO_2 (see Figure S10 in supplemental information). The highest energy level is degenerate across the two spin channels and occupied by one spin-up and spin-down electron each, indicating that this type of singlet seen both in the gas phase and evolving from the NiO_2 surface in our simulations corresponds to the $^1\Delta$ singlet where the spins are paired, giving the singlet a closed-shell character.[55,56]

DISCUSSION

Our results suggest that the redox processes in $LiNiO_2$ need to be reconsidered. Although the established ionic model assigns all redox activity to Ni and the established covalent model acknowledges that O is somewhat involved in the redox process, the extent of the O involvement in Ni–O redox seen in Figure 1 is unexpected and much greater than what previous studies have suggested. All calculations consistently suggest that what is commonly considered to be Ni-redox chemistry predominantly affects the charge state of O (see Figures 1A and 4A). Even though both Ni and O are involved in the redox process, the charge density at the Ni site barely changes on delithiation. If this effect occurred only in a Bader charge analysis, it might be considered an artifact from the choice of Bader cutoffs, not trivial for hybridized states. The DMFT calculations based on a Wannier *d-p* model, however, can separate the *d* and *p* contributions, and they confirm the constant charge state of Ni^{2+} and the changing charge state of O from −1.5 in $LiNiO_2$ to −1 in NiO_2 (and −2 in NiO). This raises the question of why the charge density changes so much more at the O site than at the Ni site. Examining the Wannier on-site energies allows for an estimation of the energy levels of the localized states. The on-site energies (see Figure 4B) show a clear separation between the Ni *d* and O *p* states (Mott-type behavior) only for the prototype rock salt NiO. In $LiNiO_2$, the difference between the O *p* states and Ni *d* states is < 1eV, promoting hybridization (as directly seen in the charge density in Figure 1C). The strong hybridization leads to pronounced splitting of the energy levels, pushing O states right up to the Fermi energy (as seen in the DOS in Figure 1B), resulting in charge transfer character. As $LiNiO_2$ is delithiated, the O states are raised in energy (Figure 4B). The Ni $e_g\pi$ states and O *p* states become degenerate in NiO_2, maximizing the splitting of the hybridized levels. Delithiation thus increasingly pushes the hybridized O states higher in energy, with charge transfer stabilizing Ni with a charge of +2 in both $LiNiO_2$ and NiO_2.

Increased covalency of the Ni–O states hence results in an increased O-redox contribution to the Ni–O redox process. The charge transfer nature of LNO is also predicted according to the criterion proposed by Zaanen, Sawatzsky, and Allen,[24,25,57] for 3*d* transition metal compounds, namely that the split between *d* and *p* states (Δ = 2 eV for LNO) is small as compared with the *d–d* split (the Coulomb repulsion U = 6 eV). Korotin et al.[18] and Foyevtsova et al.[19] also speak of ligand holes on oxygen in LNO, discussing the possibility of charge transfer behavior of LNO. Ceder and co-workers first discussed this concept in their early DFT studies of $LiCoO_2$,[25,58] highlighting the increased involvement of O as the periodic table 3*d* series is traversed. This process

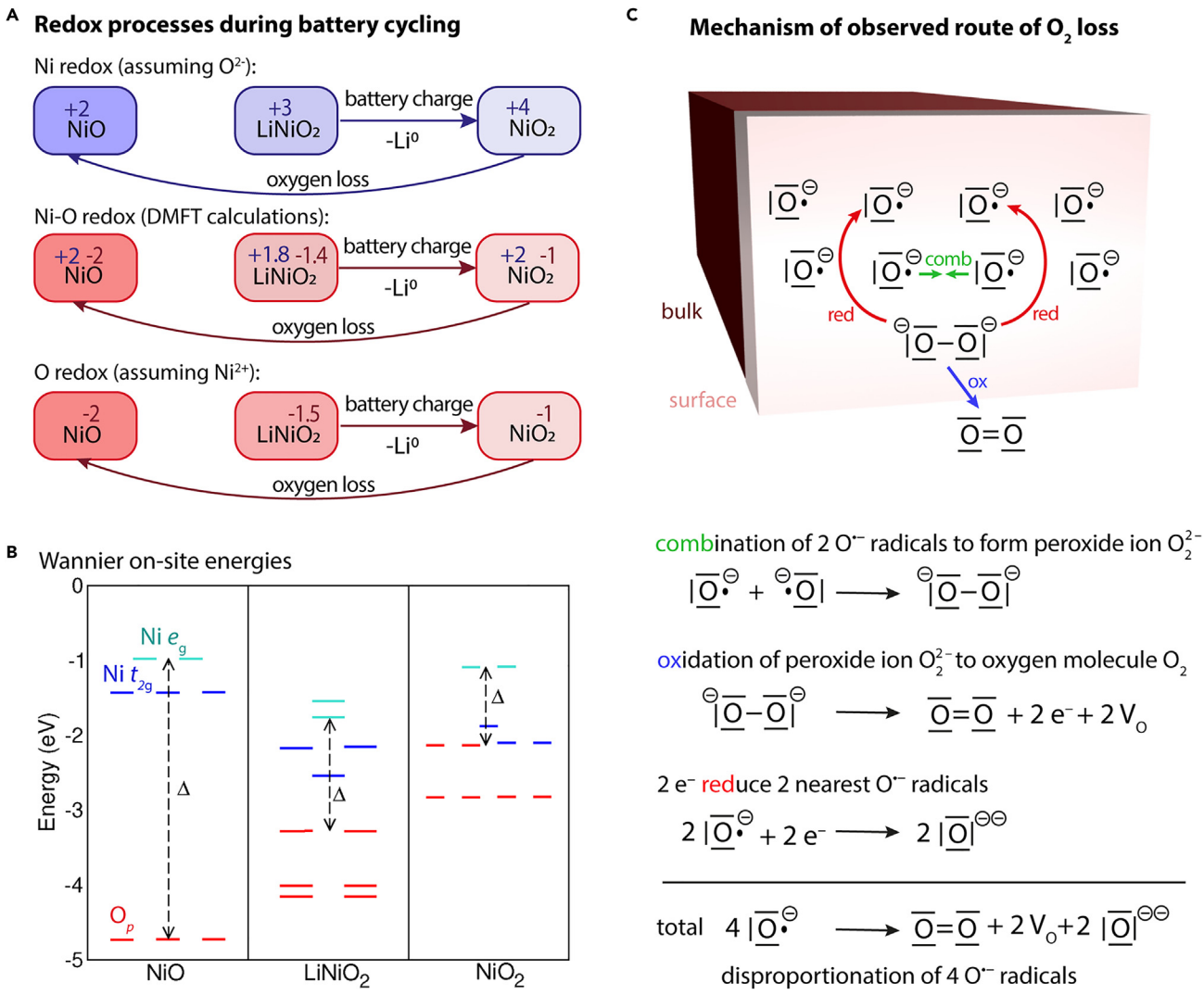

Figure 4. Proposed models of the origin and mechanism of O_2 loss in LNO

(A) Scheme illustrating the differences between the established ionic Ni redox model of LNO and the covalent Ni–O redox observed with DMFT calculations (see Figure 1), which is very close to an O redox model. The standard understanding considers Ni to undergo the greatest changes in oxidation state when a battery is cycled, from +3 in $LiNiO_2$ to +4 in NiO_2 and +2 in the prototype rock salt NiO during degradation. O is commonly considered to be less affected, mostly assuming a charge state of −2. All our DFT and DMFT simulations instead suggest that O undergoes the greatest changes in charge state, from −1.5 in $LiNiO_2$ to −1 in NiO_2 and −2 in NiO. Ni is less affected and remains in a charge state of close to +2.

(B) Wannier on-site energies for NiO, $LiNiO_2$, and NiO_2 are a measure of the energies of the localized states. The energies show a small gap Δ between the Ni *d* and O *p* states in LNO, promoting Ni−O hybridization and charge transfer behavior. The gap decreases upon delithiation. In NiO_2, the Ni *d* and O *p* states are degenerate. This causes a strong splitting of the levels of the hybridized states, presumably pushing O states close to the Fermi level. This charge transfer behavior and O-redox activity directly compromise the material's stability and promote O_2 loss.

(C) The following mechanism is derived for the route of spontaneous O_2 loss observed in AIMD simulations: (1) two oxide radicals $O^{\bullet -}$ combine to form a peroxide ion O_2^{2-}; (2) the peroxide is oxidized to an O_2 molecule, desorbs, and leaves behind two oxygen vacancies and two electrons; and (3) the 2 electrons reduce the closest $O^{\bullet -}$ radicals to O^{2-} ions. In sum, the reaction mechanism thus consists of 4 $O^{\bullet -}$ radicals disproportionating to form molecular O_2, two O^{2-} ions, and two oxygen vacancies. The rate-determining step is peroxide ion formation.

is distinct from—and often confused with[14]—the O-redox processes discussed widely in the literature, for, for example, Ni-substituted Li_2MnO_3, where the oxide anions that are oxidized, at least in some mechanisms, are in "orphan" 2*p* orbitals as found, for example, in Li–O–Li linear environments; these environments are not present in stoichiometric LNO. Huang et al.[26] have recently proposed that oxygen holes in $LiNiO_2$ could be the origin of the material's catalytic activity.

Comparing our theoretical XAS Ni *K* and O *K*-edge spectra to experimental XAS data (see Figure 2), we see excellent agreement for calculations yielding a constant Ni charge of +2 and varying O charge of −1.5 in LNO and −1 in NiO_2. Both the observed features and their evolution on delithiation agree very well with experiment, confirming the charge states proposed here. As the O *K*-edge pre-peak intensity is a measure of the Ni–O covalency and increasing covalency increases the O-redox contributions, the pre-peak also reflects the oxygen hole concentration (and directly shows the increase in holes on delithiation). The question then arises as to why XAS spectra of Ni-rich layered oxides with comparable edge shifts[15,16] have previously been considered evidence of Ni^{3+} changing to Ni^{4+}. Although it is important to remember that this process formally still involves the removal of an electron from a Ni–O-centered orbital rather than an O-centered orphan state, the results call for a brief methodological reflection on the interpretation of XAS.

XAS is a powerful method for probing local structural environments, both in terms of charge states and bonding geometries. There is, however, to date no way to deconvolute effects from the two, i.e., changes in the XAS edges could arise from changes in the charge state and/or changes in bond lengths, angles, etc.[59] Most studies to date interpret the shift of the Ni *K* edge as evidence of the Ni oxidation state changing.[11,15] The local coordination environment, however, also changes substantially upon delithiation (see Figure 2E), mainly in two regards. First, the Jahn-Teller distortions are lifted, and second, leaving aside changes in the symmetry of the bonding environment, the average Ni–O bond lengths also change on delithiation, decreasing from 2.0 Å in LNO to 1.9 Å in NiO_2. The shorter bond lengths lead to greater orbital overlap, typically manifesting itself at higher energies in the XAS spectrum. Furthermore, due to the strong Ni–O hybridization, the Ni *K* edge is also expected to be altered by changes in the O charge state. The stronger shifts in the O *K* edge, seen both computationally (Figure 2B) and experimentally (Figure 2D), illustrate that the greatest changes in electronic structure occur on O, where, in addition to the changing bond lengths, the charge state also changes substantially.

Tracing the Ni-edge shift back to changing Ni charge states is therefore by no means a clear-cut deduction, and the excellent agreement of the experimental Ni *K* and O *K* spectra and our spectra calculated at a constant Ni charge state of +2 on the contrary suggests that it is time to revisit the established interpretation. An assignment of the shift to the changing bond lengths and oxygen charge states is consistent with all our computational and reported experimental data. We propose that through a careful combination of experimental XAS and computational predictions of XAS spectra, it is possible to disentangle not only the Ni and O contributions but also the effects of charge states and local coordination environment. The combined approach thus promises to be an effective tool for assigning charge states in more covalent materials, more generally.

It can be concluded that the electrochemical redox activity of LNO stems, to a large extent, from oxidizing O, as illustrated in Figure 4A. We expect O to be strongly involved in many other oxides' redox chemistries, too, with the relative O and metal contributions depending on the degree of charge transfer character of the materials.

Identifying the central role of O redox in LNO does not open routes to enhanced capacities as the overall capacity of the hybridized Ni–O system remains constant and is also limited by the total content of lithium in the material, but it has central ramifications for the material's stability at high states of charge. If bulk Ni–O redox in LNO affects primarily the charge states of oxygen and O is oxidized on battery charging, it is not surprising that the material is unstable toward oxygen loss at high states of

charge, and similar behavior is expected for Ni-rich layered oxide cathodes in general (with the effects increasing with increasing Ni content).

The water-assisted bulk O–O-dimer formation mechanism proposed as a possible origin of the 531 eV peak in the O *K*-edge XAS spectrum at high states of charge can also be rationalized in terms of the pronounced O redox behavior of LNO. A charge analysis indicates that the dimer itself is oxidized, reducing the nearby lattice O from −1 to *ca.* −1.5, thus counteracting the oxidation of bulk O. An in-depth study will follow shortly. The dimers give rise to an XAS signal intensity around 531 eV, a frequency that is conventionally assigned to O-redox processes[60] (and they exhibit an O–O distance of *ca.* 1.2 Å, consistent with the vibronic features seen with resonant inelastic X-ray scattering, [RIXS][17,60]). As the dimer formation occurs because of O redox, the 531 eV XAS feature can technically be considered an O-redox signature. Regardless of the terminology, our ability to capture this RIXS vibronic feature at 531 eV[17] and identify it as a signature of O–O dimer formation (here due to water oxidation) further supports our ability to capture the different O redox mechanisms of the bulk phases via our calculations and accurately simulate the Ni *K* and O *K* edge XAS spectra.

We leave for a future study to clarify further why the 531 eV peak emerges at high voltages: specifically whether it requires either a critical extent of O oxidation, of electrolyte decomposition generating water, or of free space for the water molecule to enter the Li layer—or most likely a combination of these factors. Our findings further open up a bigger discussion regarding the O-redox feature reported for various materials at high states of charge, ranging from the NMCs to Li-excess materials.[60] Given that these materials differ substantially in many regards but are all oxides, the question arises if the XAS peak often assigned to O redox in some of these materials can be traced back to water reacting with oxidized lattice O to form O–O dimers. We believe this is a likely scenario that warrants a broad investigation, including a discussion of conceivable alternative origins of the high-voltage peak such as electronic quasi-particles (see Figure S7).

Methodologically, we find PBE + *U* calculations with U_{eff} = 6 eV surprisingly well suited for describing the 0 K electronic structure—particularly with respect to the charge states of LNO, NiO_2, and NiO (see Figure 1A). DMFT calculations based on a Wannier *d-p* model not only validate the trends seen with a PBE + *U* Bader charge analysis and suggest they remain valid at finite temperatures but also show excellent quantitative agreement with PBE Wannier charges. The Wannierization route for determining charges in hybridized states[29,30] in our case obtained DMFT-quality oxidation states from PBE when the basis of the Wannier model was chosen carefully (*d-p* for $LiNiO_2$ and NiO_2; *d* for NiO). It promises to be a powerful tool for quantifying charge states in battery materials more generally.

Based on our AIMD simulations of spontaneous O_2 loss from the (012) facet in NiO_2 (see Figure 3), we propose the following mechanism for the observed reaction route: (1) two oxide ion radicals $O^{\bullet-}$ combine to form a peroxide ion O_2^{2-} (see Figure 4C); (2) upon peroxide formation and desorption, the two $O^{\bullet-}$ radicals are oxidized to molecular O_2, leaving behind two oxygen vacancies and two electrons; and (3) the two electrons reduce the two closest $O^{\bullet-}$ radicals to O^{2-} ions. The latter two processes occur simultaneously. In sum, the reaction mechanism thus consists of 4 $O^{\bullet-}$ radicals disproportionating to form molecular O_2, two O^{2-} ions, and two oxygen vacancies. Whereas in metal-air batteries, the superoxide radical $O_2^{\bullet-}$ disproportionates,[31] the reaction route we observe in LNO involves the disproportionation of the oxide radical $O^{\bullet-}$, i.e., while there are parallels between the reaction

mechanisms, the disproportionating species differ according to the different battery redox chemistries. Oxide $O^{\bullet-}$ disproportionation is likely to be representative of Li-ion batteries with Ni-rich layered oxide cathodes.

After oxygen is lost, Ni migration into the Li layer is expected to result in the formation of Ni-densified surface phases (rock-salt phases).[1] We leave a more detailed investigation of the densification process for future study but point out that both Ni migration and O loss in Ni-rich oxide cathodes occur due to the thermodynamic instability of the delithiated phase. We here identify the origin of the instability of NiO_2 (and the related phenomena) to lie in the significant covalency of $LiNiO_2$ resulting in an apparent high oxidation state of O (−1) in NiO_2. A further point is the question of whether densified surface phases prohibit the further release of oxygen. Although the rock-salt phases most likely passivate the surfaces, either prohibiting or slowing down further oxygen loss, polycrystalline Ni-rich oxides are known to suffer from particle cracking,[61] which continues to expose fresh surfaces: until particle cracking can be successfully prevented, the materials are expected to continue releasing oxygen via the reported and related reaction pathways.[62–64]

The reason for the formation of singlet oxygen, we believe, lies in the ground-state singlet state of the peroxide ion. As the peroxide is oxidized to molecular oxygen, spin conservation rules favor the release of $^1O_2$. Given the strongly exergonic nature of the reaction (see Figure 3B) liberating 3 eV, $^1O_2$ is easily released in its excited state. Singlet oxygen formation in layered oxide cathodes thus follows in the footsteps of the wealth of reports of singlet oxygen formation from (mostly organic) peroxide reactions.

The final question concerns the fate of $^1O_2$ after its evolution. Does it remain in the singlet state (accounting for $^1O_2$ found experimentally[7]), react with electrolyte components (explaining the vast amounts of electrolyte oxidation products found), or deactivate into its triplet ground state? Both during the reaction and shortly after, the peroxide/O_2 molecule strongly interacts with the spins at the surface. Surface interactions, for example, enable the combination of the two $O^{\bullet-}$ radicals, each with positive spin density to the singlet peroxide in the first place—a process that would be spin forbidden for isolated radicals. Interactions of the newly formed singlet $^1O_2$ molecule with the surface will also provide routes of the otherwise spin-forbidden relaxation into triplet $^3O_2$. We leave these processes, along with those involving a direct reaction of the electrolytes with the oxidized surfaces, for future study, ideally to be addressed with dedicated multi-reference tools that can fully account for the open-shell character of the isolated O_2 molecule and excited states beyond the DFT ground state. Our work, however, shows that a low activation energy route toward singlet oxygen release occurs via the ground-state singlet state of the peroxide.

Concluding remarks

Through a rigorous charge analysis based on DFT and DMFT calculations, we have shown that the delithiation of $LiNiO_2$ to NiO_2 predominantly occurs via the oxidation of O and only causes minor changes in the charge of Ni. The Ni charge remains around +2, whether in $LiNiO_2$, NiO_2, or the prototype rock salt NiO. Instead, the oxygen charge ranges from −2 in NiO to *ca.* −1.5 in $LiNiO_2$ and −1 in NiO_2, and we propose it is the charge transfer character of LNO and the resulting dominant O redox that causes oxygen loss in Ni-rich layered cathode materials. Calculated XAS Ni *K* and O *K*-edge spectra are in excellent agreement with experimentally obtained spectra, confirming our charge analysis and suggesting that the observed Ni *K*-edge shift on delithiation stems predominantly from changes in Ni–O bond

lengths. A high-voltage feature commonly assigned to O redox could be accounted for by considering reactions of intercalated water molecules, which can combine with lattice O to form O–O dimers at high states of charge. Our AIMD simulations of the (012) facet of NiO_2 show the spontaneous evolution of O_2 molecules and the occurrence of singlet oxygen in the process. We propose the following mechanism for the observed route of O_2 loss: (1) two $O^{\bullet-}$ radicals combine to form a peroxide ion O_2^{2-}; (2) the peroxide ion is oxidized to molecular O_2, which then leaves the surface, leaving behind two oxygen vacancies and two electrons; and (3) the remaining two electrons reduce the two nearest lattice $O^{\bullet-}$ radicals to O^{2-}, the latter two steps occurring simultaneously. Overall, this means four $O^{\bullet-}$ radicals disproportionate to form O_2 and two O^{2-} ions. The reaction liberates *ca.* 3 eV. Singlet oxygen formation is caused by the singlet ground state of the peroxide ion. Spin conservation favors the release of $^1O_2$ in the excited state, which is rendered feasible through the strongly exergonic nature of the reaction. The findings presented here not only propose a revised model of redox processes in stoichiometric LNO but also offer a comprehensive atomistic understanding of the cause of oxygen loss and a reaction route forming singlet oxygen. Mitigating O_2 loss in Ni-rich cathodes and designing more reversible high-voltage cathode materials thus requires a shift in the understanding of transition metal-oxygen redox. Only if the pivotal role of O redox is acknowledged, can routes be sought to suppress oxidation—especially of the surface O—by for example adding dopants that promote more metal-centered redox rather than O-centered redox.

EXPERIMENTAL PROCEDURES

Resource availability

Lead contact

Further information and requests for resources should be directed to and will be fulfilled by the lead contact, Andrew Morris (a.j.morris.1@bham.ac.uk).

Materials availability

This study did not generate new materials.

Data and code availability

All data needed to evaluate the conclusions in the study are presented in the paper or supplemental information.

SUPPLEMENTAL INFORMATION

Supplemental information can be found online at https://doi.org/10.1016/j.joule.2023.06.017.

ACKNOWLEDGMENTS

This work was supported by the Faraday Institution degradation project (FIRG024, FIRG060). A.R.G.-S. gratefully acknowledges funding from the German National Academy of Sciences Leopoldina. We thank Angela Harper and Rebecca Nicholls for fruitful discussions. Generous computing resources were provided by the Sulis HPC service (EP/T022108/1), the University of Birmingham's BlueBEAR HPC service, and networking support by CCP-NC (EP/T026642/1), CCP9 (EP/T026375/1), and UKCP (EP/P022561/1).

AUTHOR CONTRIBUTIONS

Conceptualization, A.R.G.-S., C.P.G., and A.J.M.; methodology, A.R.G.-S., H.B., and A.J.M.; validation, A.R.G.-S., H.B., E.N.B., A.S.M., L.F.J.P., and A.J.M.;

investigation, A.R.G.-S., H.B., C.P.G., and A.J.M., writing – original draft, A.R.G.-S., H.B., and C.P.G.; writing – review & editing, H.B., A.S.M., E.N.B., L.F.J.P., C.P.G., and A.J.M.; visualization, A.R.G.-S., H.B., and A.J.M.; supervision, C.P.G. and A.J.M; funding acquisition, A.R.G.-S., L.F.J.P., C.P.G., and A.J.M.

DECLARATION OF INTERESTS

The authors declare no competing interests.

Received: December 23, 2022
Revised: April 12, 2023
Accepted: June 21, 2023
Published: July 19, 2023

REFERENCES

1. Xiao, P., Shi, T., Huang, W., and Ceder, G. (2019). Understanding surface densified phases in Ni-Rich layered compounds. ACS Energy Lett. *4*, 811–818. https://doi.org/10.1021/acsenergylett.9b00122.

2. Li, W., Erickson, E.M., and Manthiram, A. (2020). High-nickel layered oxide cathodes for lithium-based automotive batteries. Nat. Energy *5*, 26–34. https://doi.org/10.1038/s41560-019-0513-0.

3. Jung, R., Metzger, M., Maglia, F., Stinner, C., and Gasteiger, H.A. (2017). Oxygen release and its effect on the cycling stability of $LiNi_xMn_yCo_zO_2$(NMC) cathode materials for Li-ion batteries. J. Electrochem. Soc. *164*. A1361–A1377. https://doi.org/10.1149/2.0021707jes.

4. De Biasi, L., Schiele, A., Roca-Ayats, M., Garcia, G., Brezesinski, T., Hartmann, P., and Janek, J. (2019). Phase transformation behavior and stability of $LiNiO_2$ cathode material for Li-ion batteries obtained from in situ gas analysis and operando X-ray diffraction. ChemSusChem *12*, 2240–2250. https://doi.org/10.1002/cssc.201900032.

5. Das, H., Urban, A., Huang, W., and Ceder, G. (2017). First-principles simulation of the (Li–Ni–vacancy)O phase diagram and its relevance for the surface phases in Ni-Rich Li-Ion cathode materials. Chem. Mater. *29*, 7840–7851. https://doi.org/10.1021/acs.chemmater.7b02546.

6. Tornheim, A., Sharifi-Asl, S., Garcia, J.C., Bareño, J., Iddir, H., Shahbazian-Yassar, R., and Zhang, Z. (2019). Effect of electrolyte composition on rock salt surface degradation in NMC cathodes during high-voltage potentiostatic holds. Nano Energy *55*, 216–225. https://doi.org/10.1016/j.nanoen.2018.10.065.

7. Wandt, J., Freiberg, A.T.S., Ogrodnik, A., and Gasteiger, H.A. (2018). Singlet oxygen evolution from layered transition metal oxide cathode materials and its implications for lithium-ion batteries. Mater. Today *21*, 825–833. https://doi.org/10.1016/j.mattod.2018.03.037.

8. Freiberg, A.T.S., Roos, M.K., Wandt, J., de Vivie-Riedle, R., and Gasteiger, H.A. (2018). Singlet oxygen reactivity with carbonate solvents used for Li-ion battery electrolytes. J. Phys. Chem. A *122*, 8828–8839. https://doi.org/10.1021/acs.jpca.8b08079.

9. Mullinax, J.W., Bauschlicher, C.W., Jr., and Lawson, J.W. (2021). Reaction of singlet oxygen with the ethylene group: implications for electrolyte stability in Li-ion and Li-O_2 batteries. J. Phys. Chem. A *125*, 2876–2884. https://doi.org/10.1021/acs.jpca.1c00605.

10. Kong, F., Liang, C., Wang, L., Zheng, Y., Perananthan, S., Longo, R.C., Ferraris, J.P., Kim, M., and Cho, K. (2019). Kinetic stability of bulk $LiNiO_2$ and surface degradation by oxygen evolution in $LiNiO_2$ -based cathode materials. Adv. Energy Mater. *9*, 1802586. https://doi.org/10.1002/aenm.201802586.

11. Li, N., Sallis, S., Papp, J.K., Wei, J., McCloskey, B.D., Yang, W., and Tong, W. (2019). Unraveling the cationic and anionic redox reactions in a conventional layered oxide cathode. ACS Energy Lett. *4*, 2836–2842. https://doi.org/10.1021/acsenergylett.9b02147.

12. Saritas, K., Fadel, E.R., Kozinsky, B., and Grossman, J.C. (2020). Charge density and redox potential of $LiNiO_2$ using ab initio diffusion quantum Monte Carlo. J. Phys. Chem. C *124*, 5893–5901. https://doi.org/10.1021/acs.jpcc.9b10372.

13. Bianchini, M., Roca-Ayats, M., Hartmann, P., Brezesinski, T., and Janek, J. (2019). There and back again-the journey of $LiNiO_2$ as a cathode active material. Angew. Chem. Int. Ed. Engl. *58*, 10434–10458. https://doi.org/10.1002/anie.201812472.

14. Seo, D.-H., Lee, J., Urban, A., Malik, R., Kang, S., and Ceder, G. (2016). The structural and chemical origin of the oxygen redox activity in layered and cation-disordered Li-excess cathode materials. Nat. Chem. *8*, 692–697. https://doi.org/10.1038/nchem.2524.

15. Mu, L., Kan, W.H., Kuai, C., Yang, Z., Li, L., Sun, C.-J., Sainio, S., Avdeev, M., Nordlund, D., and Lin, F. (2020). Structural and electrochemical impacts of Mg/Mn dual dopants on the $LiNiO_2$ cathode in Li-metal batteries. ACS Appl. Mater. Interfaces *12*, 12874–12882. https://doi.org/10.1021/acsami.0c00111.

16. Ren, Y., Yamaguchi, R., Uchiyama, T., Orikasa, Y., Watanabe, T., Yamamoto, K., Matsunaga, T., Nishiki, Y., Mitsushima, S., and Uchimoto, Y. (2021). The effect of cation mixing in $LiNiO_2$ toward the oxygen evolution reaction. ChemElectroChem *8*, 70–76. https://doi.org/10.1002/celc.202001207.

17. Menon, A.S., Johnston, B.J., Booth, S.G., Zhang, L., Kress, K., Murdock, B.E., Paez Fajardo, G., Anthonisamy, N.N., Tapia-Ruiz, N., Agrestini, S., et al. (2023). Oxygen-redox activity in non-lithium-excess tungsten-doped $LiNiO_2$ cathode. PRX Energy *2*. https://doi.org/10.1103/PRXEnergy.2.013005.

18. Korotin, D.M., Novoselov, D., and Anisimov, V.I. (2019). Paraorbital ground state of the trivalent Ni ion in $LiNiO_2$ from DFT+DMFT calculations. Phys. Rev. B *99*. https://doi.org/10.1103/PhysRevB.99.045106.

19. Foyevtsova, K., Elfimov, I., Rottler, J., and Sawatzky, G.A. (2019). $LiNiO_2$ as a high-entropy charge- and bond-disproportionated glass. Phys. Rev. B *100*. https://doi.org/10.1103/PhysRevB.100.165104.

20. Kitchaev, D.A., Vinckeviciute, J., and Van Der Ven, A. (2021). Delocalized metal-oxygen pi-redox is the origin of anomalous nonhysteretic capacity in Li-ion and Na-ion cathode materials. J. Am. Chem. Soc. *143*, 1908–1916. https://doi.org/10.1021/jacs.0c10704.

21. Assat, G., and Tarascon, J.-M. (2018). Fundamental understanding and practical challenges of anionic redox activity in Li-ion batteries. Nat. Energy *3*, 373–386. https://doi.org/10.1038/s41560-018-0097-0.

22. Sudayama, T., Uehara, K., Mukai, T., Asakura, D., Shi, X.-M., Tsuchimoto, A., Mortemard de Boisse, B.M., Shimada, T., Watanabe, E., Harada, Y., et al. (2020). Multiorbital bond formation for stable oxygen-redox reaction in battery electrodes. Energy Environ. Sci. *13*, 1492–1500.

23. Saubanère, M., McCalla, E., Tarascon, J.-M., and Doublet, M.-L. (2016). The intriguing question of anionic redox in high-energy density cathodes for Li-ion batteries. Energy Environ. Sci. *9*, 984–991. https://doi.org/10.1039/C5EE03048J.

24. Wolverton, C., and Zunger, A. (1998). First-principles prediction of vacancy order-disorder and intercalation battery voltages in Li_xCoO_2. Phys. Rev. Lett. *81*, 606–609. https://doi.org/10.1103/PhysRevLett.81.606.

25. Aydinol, M.K., Kohan, A.F., Ceder, G., Cho, K., and Joannopoulos, J. (1997). Ab initio study of lithium intercalation in metal oxides and metal

dichalcogenides. Phys. Rev. B *56*, 1354–1365. https://doi.org/10.1103/PhysRevB.56.1354.

26. Huang, H., Chang, Y.C., Huang, Y.C., Li, L., Komarek, A.C., Tjeng, L.H., Orikasa, Y., Pao, C.W., Chan, T.S., Chen, J.M., et al. (2023). Unusual double ligand holes as catalytic active sites in $LiNiO_2$. Nat. Commun. *14*, 2112. https://doi.org/10.1038/s41467-023-37775-4.

27. Mulliken, R.S. (1955). Electronic population analysis on LCAO–MO molecular wave functions. I. J. Chem. Phys. *23*, 1833–1840. https://doi.org/10.1063/1.1740588.

28. Bader, R.F.W. (1985). Atoms in molecules. Acc. Chem. Res. *18*, 9–15. https://doi.org/10.1021/Ar00109a003.

29. Reeves, K.G., and Kanai, Y. (2014). Theoretical oxidation state analysis of Ru-$(bpy)_3$: influence of water solvation and Hubbard correction in first-principles calculations. J. Chem. Phys. *141*, 024305. https://doi.org/10.1063/1.4886406.

30. Quan, Y., and Pickett, W.E. (2015). Analysis of charge states in the mixed-valent ionic insulator AgO. Phys. Rev. B *91*. https://doi.org/10.1103/PhysRevB.91.035121.

31. Houchins, G., Pande, V., and Viswanathan, V. (2020). Mechanism for singlet oxygen production in Li-ion and metal–air batteries. ACS Energy Lett. *5*, 1893–1899. https://doi.org/10.1021/acsenergylett.0c00595.

32. Zhu, J., and Chen, G. (2019). Single-crystal based studies for correlating the properties and high-voltage performance of Li $[Ni_xMn_yCo_{1-x-y}]O_2$ cathodes. J. Mater. Chem. A *7*, 5463–5474. https://doi.org/10.1039/C8TA10329A.

33. Garcia, J.C., Bareño, J., Yan, J., Chen, G., Hauser, A., Croy, J.R., and Iddir, H. (2017). Surface structure, morphology, and stability of $Li(Ni_{1/3}Mn_{1/3}Co_{1/3})O_2$ cathode material. J. Phys. Chem. C *121*, 8290–8299. https://doi.org/10.1021/acs.jpcc.7b00896.

34. Kramer, D., and Ceder, G. (2009). Tailoring the morphology of $LiCoO_2$: a first principles study. Chem. Mater. *21*, 3799–3809. https://doi.org/10.1021/cm9008943.

35. Cho, E., Seo, S.-W., and Min, K. (2017). Theoretical prediction of surface stability and morphology of $LiNiO_2$ cathode for Li ion batteries. ACS Appl. Mater. Interfaces *9*, 33257–33266. https://doi.org/10.1021/acsami.7b08563.

36. Cheng, J., Mu, L., Wang, C., Yang, Z., Xin, H.L., Lin, F., and Persson, K.A. (2020). Enhancing surface oxygen retention through theory-guided doping selection in $Li_{1-x}NiO_2$ for next-generation lithium-ion batteries. J. Mater. Chem. A *8*, 23293–23303. https://doi.org/10.1039/D0TA07706B.

37. Xu, C., Märker, K., Lee, J., Mahadevegowda, A., Reeves, P.J., Day, S.J., Groh, M.F., Emge, S.P., Ducati, C., Layla Mehdi, B., et al. (2021). Bulk fatigue induced by surface reconstruction in layered Ni-rich cathodes for Li-ion batteries. Nat. Mater. *20*, 84–92. https://doi.org/10.1038/s41563-020-0767-8.

38. Rinkel, B.L.D., Hall, D.S., Temprano, I., and Grey, C.P. (2020). Electrolyte oxidation pathways in lithium-ion batteries. J. Am. Chem. Soc. *142*, 15058–15074. https://doi.org/10.1021/jacs.0c06363.

39. Reynaud, F., Ghorayeb, A.M., Ksari, Y., Menguy, N., Stepanov, A., and Delmas, C. (2000). On the 240 K anomaly in the magnetic properties of $LiNiO_2$. Eur. Phys. J. B *14*, 83–90. https://doi.org/10.1007/s100510050109.

40. Hirota, K., Nakazawa, Y., and Ishikawa, M. (1991). Magnetic properties of the S=1/2 antiferromagnetic triangular lattice $LiNiO_2$. J. Phys.: Condens. Matter *3*, 4721–4730. https://doi.org/10.1088/0953-8984/3/25/017.

41. Hirota, K., Nakazawa, Y., and Ishikawa, M. (1990). Specific heat and susceptibility of the S= 1/2 triangular lattice magnet $LiNiO_2$. J. Magn. Magn. Mater. *90–91*, 279–280. https://doi.org/10.1016/S0304-8853(10)80099-X.

42. Molenda, J., Wilk, P., and Marzec, J. (2002). Structural, electrical and electrochemical properties of $LiNiO_2$. Solid State Ionics *146*, 73–79. https://doi.org/10.1016/S0167-2738(01)00992-4.

43. Anisimov, V.I., Zaanen, J., and Andersen, O.K. (1991). Band theory and Mott insulators: Hubbard *U* instead of Stoner I. Phys. Rev. B Condens. Matter *44*, 943–954. https://doi.org/10.1103/physrevb.44.943.

44. Anisimov, V.I., Solovyev, I.V., Korotin, M.A., Czyzyk, M.T., and Sawatzky, G.A. (1993). Density-functional theory and NiO photoemission spectra. Phys. Rev. B Condens. Matter *48*, 16929–16934. https://doi.org/10.1103/physrevb.48.16929.

45. Radin, M.D., and Van Der Ven, A. (2018). Simulating charge, spin, and orbital ordering: application to Jahn–teller distortions in layered transition-metal oxides. Chem. Mater. *30*, 607–618. https://doi.org/10.1021/acs.chemmater.7b03080.

46. Rougier, A., Delmas, C., and Chadwick, A.V. (1995). Non-cooperative Jahn-Teller effect in $LiNiO_2$: an EXAFS study. Solid State Commun. *94*, 123–127. https://doi.org/10.1016/0038-1098(95)00020-8.

47. Lee, C., Yokoyama, Y., Kondo, Y., Miyahara, Y., Miyazaki, K., and Abe, T. (2020). What insertion species is electrochemically intercalated into the $LiNiO_2$ electrode in aqueous solutions? J. Power Sources *477*, 229036. https://doi.org/10.1016/j.jpowsour.2020.229036.

48. Rinkel, B.L.D., Vivek, J.P., Garcia-Araez, N., and Grey, C.P. (2022). Two electrolyte decomposition pathways at nickel-rich cathode surfaces in lithium-ion batteries. Energy Environ. Sci. *15*, 3416–3438.

49. Benedek, R., Thackeray, M.M., and van de Walle, A. (2008). Free energy for protonation reaction in lithium-ion battery cathode materials. Chem. Mater. *20*, 5485–5490. https://doi.org/10.1021/cm703042r.

50. Gu, X., Liu, J.-l., Yang, J.-h., Xiang, H.-j., Gong, X.-g., and Xia, Y.-y. (2011). First-principles study of H^+ intercalation in layer-structured $LiCoO_2$. J. Phys. Chem. C *115*, 12672–12676. https://doi.org/10.1021/jp202846p.

51. Ruff, Z., Coates, C.S., Märker, K., Mahadevegowda, A., Xu, C., Penrod, M.E., Ducati, C., and Grey, C.P. (2023). O3 to O1 phase transitions in highly delithiated NMC811 at elevated temperatures. Chem. Mater. https://doi.org/10.1021/acs.chemmater.3c00307.

52. Lu, Z., and Dahn, J.R. (2001). Intercalation of water in P2, T2 and O2 structure A_z $[Co_xNi_{1/3-x}Mn_{2/3}]O_2$. Chem. Mater. *13*, 1252–1257.

53. Fueno, H., Takenaka, Y., and Tanaka, K. (2011). Theoretical study on energy transfer from the excited C_{60} to molecular oxygen. Opt. Spectrosc. *111*, 248–256. https://doi.org/10.1134/S0030400X11080133.

54. Kearns, D.R. (1971). Physical and chemical properties of singlet molecular oxygen. Chem. Rev. *71*, 395–427. https://doi.org/10.1021/cr60272a004.

55. Ponra, A., Etindele, A.J., Motapon, O., and Casida, M.E. (2021). Practical treatment of singlet oxygen with density-functional theory and the multiplet-sum method. Theor. Chem. Acc. *140*. https://doi.org/10.1007/s00214-021-02852-8.

56. Stuyver, T., Chen, B., Zeng, T., Geerlings, P., De Proft, F., and Hoffmann, R. (2019). Do diradicals behave like radicals? Chem. Rev. *119*, 11291–11351. https://doi.org/10.1021/acs.chemrev.9b00260.

57. Zaanen, J., Sawatzky, G.A., and Allen, J.W. (1985). Band gaps and electronic structure of transition-metal compounds. Phys. Rev. Lett. *55*, 418–421. https://doi.org/10.1103/PhysRevLett.55.418.

58. Ceder, G., Chiang, Y.-M., Sadoway, D.R., Aydinol, M.K., Jang, Y.-I., and Huang, B. (1998). Identification of cathode materials for lithium batteries guided by first-principles calculations. Nature *392*, 694–696. https://doi.org/10.1038/33647.

59. Taftø, J., and Krivanek, O.L. (1982). Site-specific valence determination by electron energy-loss spectroscopy. Phys. Rev. Lett. *48*, 560–563. https://doi.org/10.1103/PhysRevLett.48.560.

60. House, R.A., Marie, J.-J., Pérez-Osorio, M.A., Rees, G.J., Boivin, E., and Bruce, P.G. (2021). The role of O_2 in O-redox cathodes for Li-ion batteries. Nat. Energy *6*, 781–789. https://doi.org/10.1038/s41560-021-00780-2.

61. Yoon, C.S., Jun, D.-W., Myung, S.-T., and Sun, Y.-K. (2017). Structural stability of $LiNiO_2$ cycled above 4.2 V. ACS Energy Lett. *2*, 1150–1155. https://doi.org/10.1021/acsenergylett.7b00304.

62. Adam, W., Kazakov, D.V., and Kazakov, V.P. (2005). Singlet-oxygen chemiluminescence in peroxide reactions. Chem. Rev. *105*, 3371–3387. https://doi.org/10.1021/cr0300035.

63. Evans, D.F., and Upton, M.W. (1985). Studies on singlet oxygen in aqueous solution. Part 3. The decomposition of peroxy-acids. J. Chem. Soc. Dalton Trans. *6*, 1151–1153. https://doi.org/10.1039/DT9850001151.

64. Held, A.M., Halko, D.J., and Hurst, J.K. (1978). Mechanisms of chlorine oxidation of hydrogen peroxide. J. Am. Chem. Soc. *100*, 5732–5740. https://doi.org/10.1021/ja00486a025.